Characterization of Flame Front Wrinkling in a Highly Pressure-Charged Spark Ignition Engine

Wankang Zhang[a], Mohamed E. Morsy[a,b], Zhengyang Ling[a], Junfeng Yang[a*]

[a] School of Mechanical Engineering, University of Leeds, Leeds, LS2 9JT, UK.

[b] Faculty of Engineering at El-Mattaria, University of Helwan, Cairo 11718, Egypt.

**Corresponding Author: J.Yang@leeds.ac.uk*

Abstract

Particle Image Velocimetry (PIV) technique has been employed to investigate turbulent flame propagation in a relatively quiescent, optically accessed, boosted, two-stroke spark ignition engine. Turbulence scales and flame structure have been characterized based on Fourier analysis of an independent stationary coordinate at elevated pressures. Analysis shows that turbulence, with an initial rms value of u', is modified by flames, and the strong induced velocity field ahead of it. As the flame grows, the persistence of larger scale structures as well as smaller scale wrinkling is apparent. Power spectral density (PSD) of flame wrinkling exhibit the same general trend under different operating conditions. These are in a good agreement with the previous data measured from other rigs (i.e. burners and bombs), which featured lower pressures. These functions have been normalized by terms of wrinkling parameters and other turbulence parameters. General PSD functions are developed. These can predict the flame wrinkling behavior at low and high pressures, in different experimental apparatuses.

Keywords: Flame front analysis; PIV, Strongly Pressure-Charged; SI Engine.

1. Introduction

To improve the vehicle fuel economy, engine downsizing concepts have been developed and considered to be promising solutions [1]. However, reducing the swept volume usually sacrifices the engine torque and power. To obtain the same engine torque, the use of air boosting seems to be the best solution to adopt. Thus, a strongly charged spark ignition (SI) engine became the trend in engine development. One of the challenges is that the higher effective compression ratio achieved by supercharging raises the charge pressure and temperature and consequently increases the turbulence level which has a significant effect of the flame wrinkling and hence on the turbulent burning velocity [2, 3]. Furthermore, the propagation history of a premixed turbulent flame has great impact on the engine performance and efficiency. Consequently, a better understanding of the flame wrinkling and all related turbulence characteristics could allow the optimization of boosted spark-ignition engines. This paper presents the results of a study carried out for this purpose using a high repetition rate Particle Image Velocimetry (PIV) technique to characterise the turbulent flame structures in a highly supercharged engine.

The presence of turbulence in cold unburned gas distorts the flame surface, resulting in a locally wrinkled flame structure, which favours mixture burning rate. One expects a highly wrinkled flame surface due to the high stretch rate induced by turbulent eddies. With increasing pressure appearance of cellular structures increase flame wrinkling in addition to what is achieved by turbulence. Wirth et al. [4] and Hicks et al. [5] investigated the turbulent flame structure in spark ignition engines and attempted to pinpoint the inherent link between turbulence and flame wrinkling by comparing the spectrum of flame wrinkling with the energy spectrum of turbulence. Atashkari et al. [6] investigated the premixed flame wrinkling over fairly wide range of rigs (burner, constant volume combustion vessel and engine) and pressures (1-17 bar). Atashkari et al. observed that pressure has little effect on the shape of flame spectrum, and suggested a generality of turbulent premixed flame wrinkling in terms of dimensionless groups. This is restricted by the available pressure range and flame contour resolution (> 0.2 mm). The modern SI engines usually feature a higher compression ratio and a boosted intake system to achieve higher pressure (~ 30 bar) at spark timing, which favors a higher output power and thermal efficiency.

As mentioned before, wrinkles become smaller at higher pressures. It is therefore worth investigating whether this generality is still valid for a much higher-pressure system using higher resolution imaging system.

To obtain accurate flame contours and turbulence characteristics, fast laser technology and high-speed imaging system are essential. Laser tomography is widely used to capture flame front since 1980s [7]. Taking the advantage of rapid development of laser tomographic method and digital camera over decades, numerous experimental studies have been conducted to get better understanding of the turbulent premixed flame wrinkling. Takeno et al. [8] investigated the fractal characterisation of lean CH_4-air turbulent premixed flame surface using laser tomography technique and had not found a direct link between fractal-like character flow turbulence. By employing Stepping Caliper Method, Shepherd et al. [9] were able to accurately determine the fractal parameters (e.g. fractal dimension, inner and outer cutoffs) from digitized flame boundaries of premixed turbulent CH_4-air flames obtained by the Mie scattering. Gülder and Smallwood [10] evaluated the previous studies of flame surface wrinkling on 2D flame front imaging that were obtained by Mie Scattering and OH Laser Induced Fluorescence(LIF) methods, and derived an improved formulation of inner cutoff scale which represents the smallest scale for the interaction of turbulent eddies with the premixed flame front. Haq et al. [11] studied the wrinkling and curvature of premixed iso-octane and methane-air flames in a fan-stirred vessel in laminar conditions and turbulent flow fields at 1 and 5 bar using OH LIF sheet images, and found flames exhibited more curvature at high pressure. Bradley et al. [12] studied the induced flow velocity by combustion in a fan-stirred vessel using PIV technique. They concluded that, the existing fan-stirred turbulence at the wrinkled flame front is significantly enhanced by the high expansion velocity induced by combustion beyond that front. Cohé et al. [13] conducted fractal analysis of hydrogen-enriched CH_4–air premixed flames from a turbulent Bunsen burner at 1-9 bar using planar Mie scattering tomography, and observed that turbulent length scales play a significant role in the fractalization of premixed turbulent flames. The finer structures and increase of curvature of flame front was further reported under the high pressure conditions. The fractal analysis for flame front wrinkles in spark ignition engines were conducted experimentally using 2D laser-light sheet technique in [14-16]. However, none of them analysed the spectrum of flame wrinkling.

Kobayashi and Kawazoe [17] studied the flame winkles of CH_4/air and C_3H_8/air mixtures in a Bunsen-type burner at pressure 1-10 bar using Planar LIF (PLIF), and confirmed that small-scale winkles dominate at high pressure environment. Gashi et al. [18] studied the curvature and wrinkling of premixed flame kernels for CH_4/air and H_2/air mixtures in a combustion bomb using 2D PLIF technique, Weiβ et al. [19] employed PIV to investigate the premixed flame front of CH_4/air, C_3H_8/air and H_2/air mixtures in a combustion bomb under atmospheric conditions. Kheirkhah and Gülder [20] employed a similar technique to study the characteristics of turbulent premixed flame fronts of CH_4/air mixtures in a V-shape burner under atmospheric condition. They concluded that the Power Spectrum Density (PSD) of the flame wrinkling exhibits a power-law relation with the wavenumber. Ling [21] employed a boosted optical SI engine and conducted flame spectral analysis of iso-octane/air mixtures using a slow PIV (maximum repetition rate 10 Hz). Ling also reported a power-law expression of PSD of flame wrinkling at high pressure. Ichikawa et al. [22] investigated the premixed flame surface density of CH_4/NH_3/air mixtures in a nozzle burner at pressure up to 5 bar using PLIF.

Although, considerable efforts have tried to get better understanding of the turbulent premixed flame wrinkling, none of them except that Ling [21] used the spectrum analysis to describe the flame wrinkling under high pressures, encountered in modern strongly charged engines. However, in Ling's boosted engine measurements, only one flow field at the Top Dead Centre (TDC) was captured in each test. This omits the temporal developments of the wrinkling parameters. Experimental study on high pressure combustion remains challenging and data is scarce. There is still considerable scope for validation and improvement on the aforementioned generality of flame wrinkling over a wider range of pressures and turbulence.

The present work aims to investigate the characteristics of turbulent premixed flames at high pressures. The wrinkling parameters obtained from this work together with previous measurements confirm more confidently whether the wrinkling generality is valid over a wide range of pressures. To this end, a naturally aspirated Leeds University Ported Optical Engine-Version 2 with Disc-head (LUPOE2-D) was modified so that the peak motoring pressure could reach high values over 30 bar, to simulate the in-cylinder condition of super- and turbo- charged engines. A series of 2D planer Mie scattering measurements were recorded to study the detailed structure of flame surface wrinkling. The turbulence parameters inside the LUPOE-2D was measured using a high speed PIV system.

The rest of this paper is organized as follows. In Section 2, the experimental devices and data processing are described, whilst the results and discussion are presented in Section 3. Finally, Section 4 is devoted to concluding remarks.

2. Experimental Methodology

2.1. Research Engine

The original LUPOE2-D was derived from a naturally aspirated two-stroke single cylinder engine. This engine was modified to include a boosting system so that the peak motoring pressure could reach high pressure value (~ 30 bar), close to those encountered in the super- and turbo- charged engines. The LUPOE2-D engine is consisted of one-cylinder with full-bore top and side optical access, dynamometer drive, air and fuel suppliers, data acquisition and control systems. Figure 1 shows Photograph of this engine and its peripheral equipment. The engine was driven by a dynamometer to achieve desired operating speeds. It had a flywheel to store the high angular momentum required to keep the engine running smoothly during compression and expansion strokes. A shaft encoder was employed to provide the control unit with reference timing signals at TDC.

The original cylinder head was replaced by a newly designed optical head (shown in Fig. 1) to achieve a full-bore optical access. Which comprises of a top window, two side windows, a spark plug and a dynamic pressure transducer. The top window provided a full top view of the combustion process and contained a custom-built spark plug which sat in the centre of the bore. The spark electrodes protruded about 3 mm below the lower surface of the top window. The side windows allowed a laser sheet to pass through the bore for PIV measurement and flame sheet imaging. Two intake ports of rectangular cross section and an exhaust passage consisting of a colander, four rings of circular exhaust holes drilled in the engine liner, communicating with a void between the liner and barrel leading to one exhaust duct as shown in Fig. 1. The time of the ports opening and closure are controlled by the movement of the modified flat piston. For all investigations described in this paper, the isooctane fuel was used with two fuel-air equivalence ratios of 0.8 and 1.0. The flame structures were investigated at two engine speeds, 750 and 1500 RPM. The LUPOE2-D engine specifications are listed in Tables 1 and 2. More information about this engine, its air-fuel system and the data acquisition system can be found in [23].

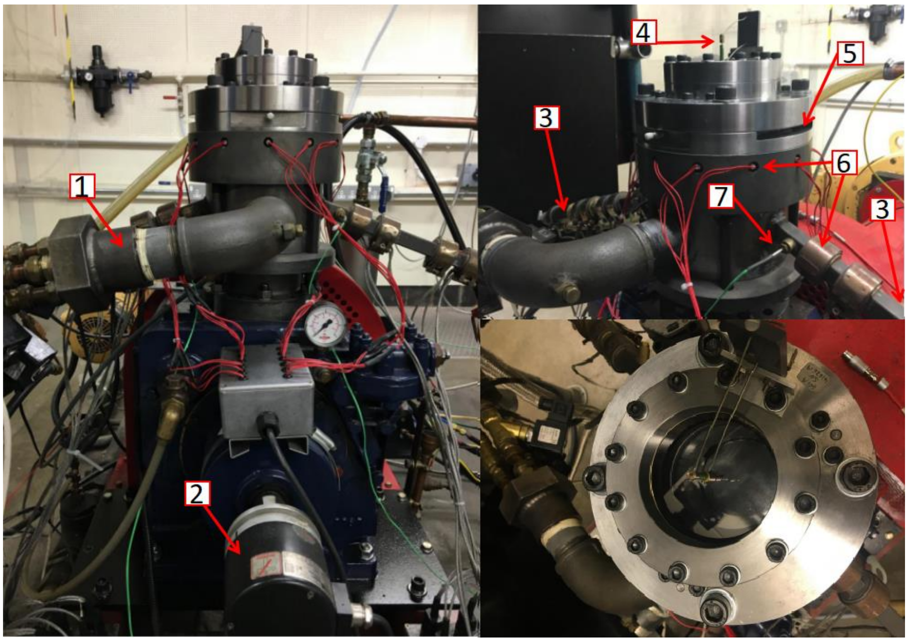

Fig. 1: Photograph of LUPOE2-D engine and its peripheral components:1 - exhaust pipe 2 - shaft encoder 3 - intake pipe 4 - spark plug 5 - side window 6 - heater 7 - thermocouple

Table 1: LUPOE2-D specifications and operating conditions.

Engine Head	Disc
Bore [mm]	80
Stroke [mm]	110
Connect Rod Length [mm]	232
Clearance Height [mm]	7.5
Compression Ratio	11.38
Numbers of Exhaust Holes	30
Inlet Ports Opening/Closure CA [deg]	107.8
Exhaust Ports Opening/Closure CA [deg]	127.6
Available Engine Speed [RPM]	750, 1500
Fuel	Iso-octane (purity grade > 99% by volume)
Equivalence ratio, ϕ	0.8, 1.0

Table 2: LUPOE2-D intake condition and spark timing.

Engine Speed rpm	Mixture strength ϕ	Intake pressure bar	Intake temperature K	Spark Timing CAD BTDC
750	0.8	1.58	318	6
750	1.0	1.65	323	3
1500	0.8	1.52	313	10
1500	1.0	1.54	318	5

The operation characteristics of LUPOE-2D under different conditions are presented in Tables 3. Figure 2 shows the in-cylinder pressure traces for engine speeds 750 and 1500 RPM, during motored and firing cycles. Those curves, in Fig. 2, are mean of 50 cycles at each condition. The intake temperature and pressure (T&P) were well adjusted in order to achieve identical T&P before the spark engaged. Spark timing was controlled in order to maintain nearly constant T&P during the flame propagation. The present work focuses on a fully developed flame radius range of (12 mm < r < 18 mm). This is corresponding to a mass fraction burned (2%-7%), as shown in Fig. 3. In addition, this radius range ensures a minimal influence of spark and cylinder wall. Turbulence parameters, u' and L, were reported in Section 3.1. Maximum attained values L_{ak} and a'_k , in Figs. 12 c)&d) were used here for the flame wrinkling parameters. The laminar burning velocity, u_l, for iso-octane/air mixture was calculated at temperature 650 K and pressure 30 (unburnt gas property at TDC) using the method reported by Metghalchi and Keck [24]. A formulation of inner cutoff, $\delta_l K_a^{-1/2}$ reported in [10] was adopted herein. K_a and δ_l represent the Karlovitz number and is the laminar flame thickness, respectively.

Table 3: Operating characteristics of LUPOE-2D

Engine speed (RPM)	ϕ	u' (ms^{-1})	L at 10° aTDC (mm)	u_l (ms^{-1})	u'/u_l	L_{ak} (mm)	a'_k (mm)	Inner cutoff (mm)
750	0.8	0.75	3.5	0.57	1.32	8.1	1.7	0.044
750	1.0	0.75	3.5	0.79	0.95	8.1	1.79	0.044
1500	0.8	1.2	3.5	0.57	2.1	9.8	2.5	0.031
1500	1.0	1.2	3.5	0.79	1.51	7.2	1.8	0.031

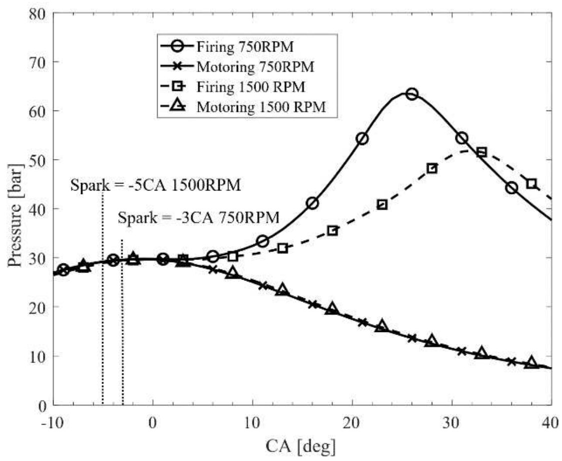

Fig. 2 shows the in-cylinder pressure traces versus crank angle, during motored and firing cycles for engine speeds 750 and 1500 RPM. Curves are mean of 50 cycles at each condition.

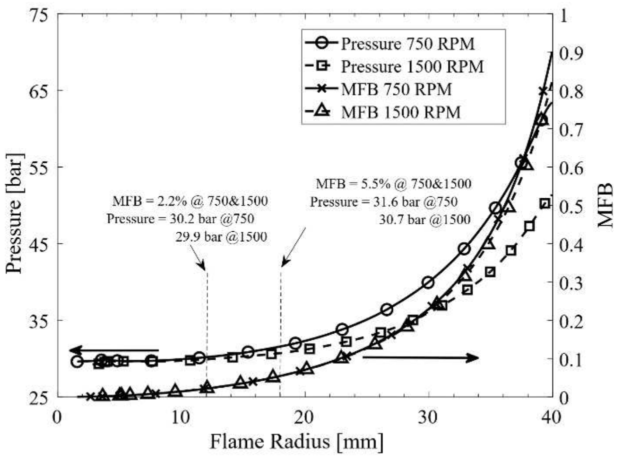

Fig. 3 Shows the pressure and MFB variation with flame radius at 750 and 1500 RPM.

2.2. PIV system

Particle Image Velocimetry system was employed to obtain the flow velocity and recording the flame propagation inside the LUPOE-2D engine under different operating conditions. This system is consisted of three parts: a single cavity copper vapour laser, the tracer particles generator, and a high-speed camera, as indicated in Fig. 4. The single cavity copper vapour laser produced laser light at 511 nm (green) and 578 nm (yellow) with a pulse energy of about 1 mJ, at a repetition rate of 10 kHz. The diameter of the laser beam was approximately 25 mm, it passed through a series of lenses to form a thin laser sheet, as shown in Fig. 4. The laser sheet passes through the middle surface of the clearance volume, i.e. positioned 4±0.5 mm below the lower surface of the top optical window. The measuring system was comprised of a spherical convex lens of -150 mm and cylindrical lens of +150 mm focal length. These created a laser sheet about 0.5 mm thick to illuminate the uniformly dispersed seeding particles in the flow.

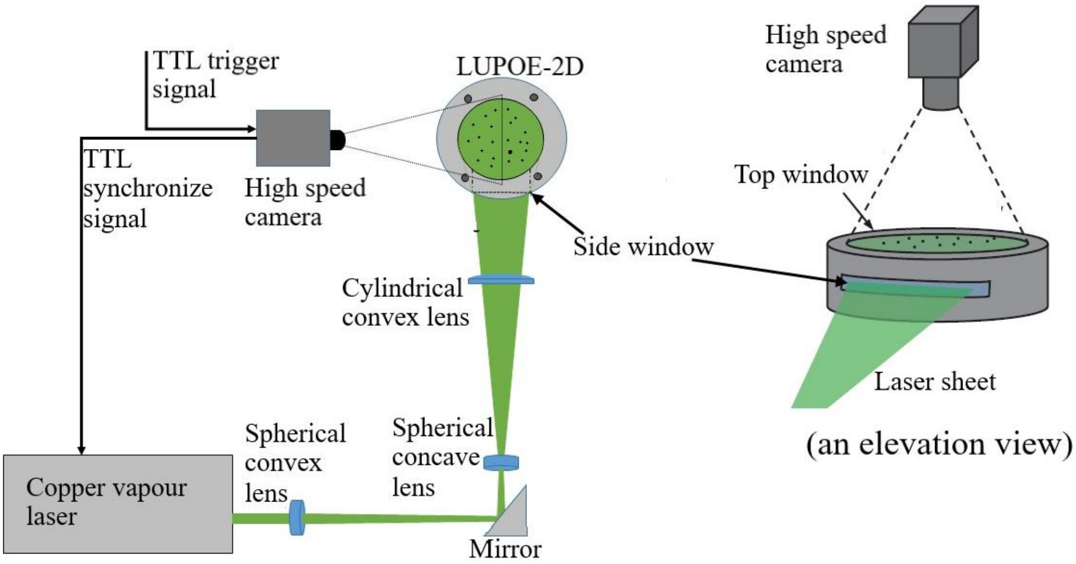

Fig. 4: A schematic diagram of PIV setup in this study

Refined olive oil was used as tracer particles in this study due to its low cost and relatively low relaxation time. The particles were supplied at the downstream of the surge tank where allows sufficient mixing to form a uniform particle distribution before feeding to the engine. The tracer particle size was less than 5 μm to minimize its lagging effect on the main gas flow. In addition, only a small amount of olive oil was used to ensure a negligible influence of the oil burning on engine combustion.

A high-speed camera 'Photron AR-X', perpendicular to the laser sheet, recorded a 12-bit image pair of spatial resolution 512 x 512 pixels at a frequency of 10 kHz. For the full-bore view, the pixel size in this study was about 0.16 mm. For a zoomed in flame study, the pixel size was approximately 0.065 mm from calibration. The camera shutter time was about 4 μs to eliminate influence from the light emitted from chemical reaction to form a great contrast between unburned and burned region. Summary of the imaging system settings are listed in Table 4.

Table 4: The imaging system settings.

Camera	Photron APX RS
Spatial Resolution [Pixel]	512 x 512
Pixel Resolution [mm/pixel]	0.16 x 0.16 (full-bore view) or 0.065 x 0.065 (1/4 bore view)
Filming Speed [kHz]	10
Exposure Time [s]	1/253000
Interrogation Window [Pixel]	32 x 32

Interrogation Window (zoomed-in) [Pixel]	64 x 64
Overlap	50%

Prior to the experiments, the camera was calibrated. A circular calibration plate, to which the grid paper with equidistant dots were attached, was used for the calibration. First, the camera was focused manually on the measurement plane, using this plate and then using the seeding particles themselves. The standard deviation of the detected dots was $\sigma = 0.098$, calculated by a MATLAB script. Using these procedures, the image resolution for calibration was 0.16 mm/pixel. Segment linear calibration image distortion far less than 1%, which has negligible effect on PIV result. Dot sheet with a radius of 40 mm and 5 mm distance between dots was used for the calibration. The dot centre was detected using a MATLAB code, and treated as a reference pixel. Therefore, the real distance was a function of the distance between reference pixels in the calibration image. To obtain accurate results, several aspects were taken into consideration during installing and employing the PIV system. In the present work, the optimal size of initial interrogation window was 32 and 64 for non-zoomed in setup and zoomed in setup, respectively. The corresponding average number of tracer particles in the interrogation window was kept between 10 and 34. The maximum error of the PlV results was 1.2% under different experimental conditions, which corresponds to the absolute error of 0.38 pixel.

2.3. Data Post-Processing

A Fast Fourier Transform (FFT) based on cross-correlation method [25] was used to derive the velocity vectors from the PIV images. By correlating the FFT frequency domain of intensity field within an interrogation area of two consecutive images, the mean displacement is calculated for that area. A multi-pass approach [26] was applied to improve the PIV accuracy, starting with the interrogation window size of 32 x 32 pixels and 50% of overlap. For firing cycle, the maximum speed was approximately 12 m/s (equivalent to 7.5 pixel/frame); whilst it was 3.3 m/s for motoring cycles (2.1 pixel/frame). Each pass was one- half the size of interrogation window to accommodate with the detailed particle movement. Peak-locking was avoided by choosing one-dimensional 2x3-point Gaussian function for high sub-pixel accuracy. The particle drop-out is determined by the interrogation window size. And initial window size 32x32 was chosen to ensure the maximum particle displacement was less ¼ interrogation window size. The velocity vector for that interrogation area was then determined using the time separation between the two illuminations and located at the centre of the interrogation area. By applying this procedure for all the interrogation areas, a 2-D velocity vector field is produced. This processing algorithm called “PIV-Lab”. More details about this algorithm can be found in [26]. The time separation between two consecutive images with was 0.1 ms. A sample of the PIV vector field collected in this study and its magnitude map at TDC at an engine speed 750 RPM motoring cycle is shown in Fig. 5. For clarity, the vectors are displayed in Fig. 5a. Reuss [27], employed a 2D-PIV to measure the characteristics of large-scale flow-structures at TDC in a motored, two-valve, four-stroke engine using highly directed flow by a shrouded valve and a relatively undirected flow using a standard valve. For the undirected flow, it was concluded that none of cycles had the appearance of the ensemble mean and the instantaneous velocity vectors had no specific pattern. Similar observation. This is in a good agreement with the results shown in Fig. 5.

The Root-Mean-Square turbulent velocity components, $u'_x(x,y)$ and $u'_y(x,y)$, in the x and y-directions, respectively, are calculated using the following expression [28]:

$$u'_x(x,y) = \sqrt{\frac{1}{N}\sum_{i=1}^{N}[U_x(x,y,i) - \overline{U_x}(x,y)]^2} \quad (1)$$

$$u'_y(x,y) = \sqrt{\frac{1}{N}\sum_{i=1}^{N}\left[U_y(x,y,i) - \overline{U_y}(x,y)\right]^2} \quad (2)$$

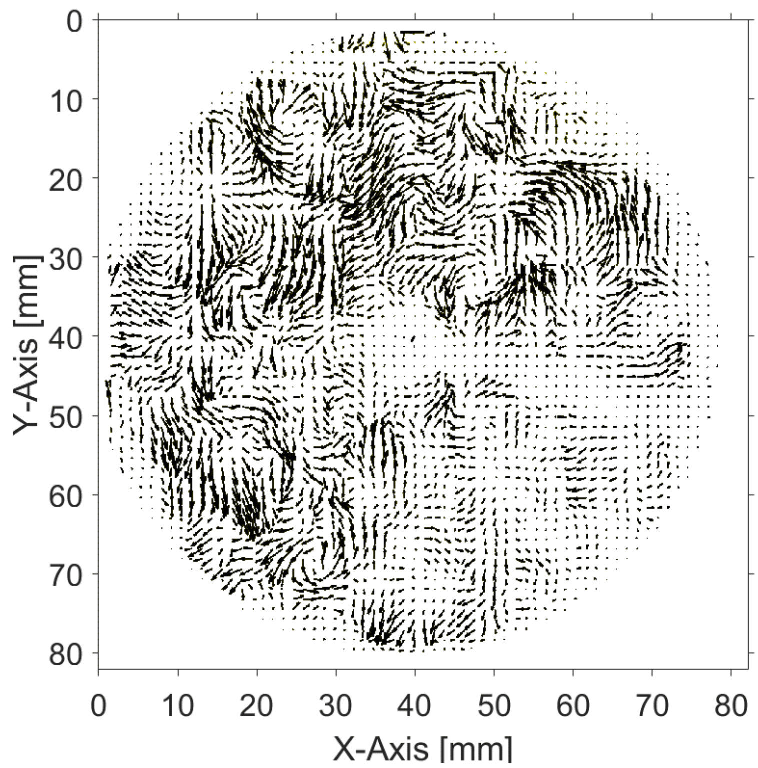

(a)

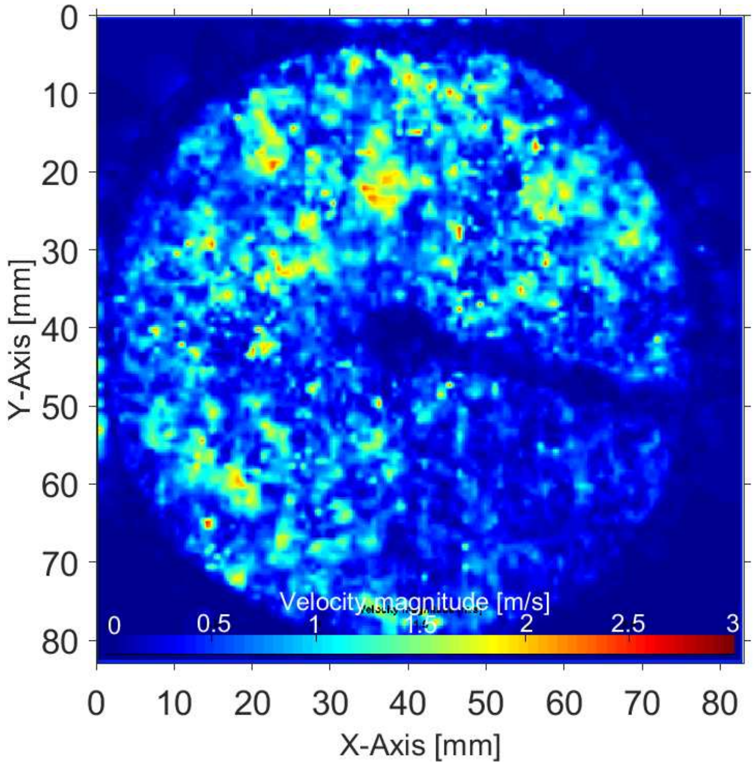

(b)

Fig. 5: A snapshot of the flow velocity field captured by PIV at TDC position at an engine speed of 750 RPM motoring cycle, illustrated in the form of (a) velocity vector, and (b) velocity magnitude.

where $U_x(x,y,i)$ and $U_y(x,y,i)$ are the instantaneous velocity components at the point (x, y) in the i-th cycle. $\overline{U_x}(x,y)$ and $\overline{U_y}(x,y)$ are ensemble averaged velocities from total number of motoring cycles, N (=50). The turbulence RMS velocity $u'(x,y)$ at each point is defined as the quadratic mean of its components. A mean value of turbulence RMS velocity field, u'_x and u'_y, at a single time instance can then be obtained by taking an arithmetic average of $u'_x(x,y)$and $u'_y(x,y)$, respectively, from the whole flow field.

Depending on the velocity direction, four integral length scales, L_{xl}, L_{xt}, L_{yl} and L_{yt}, were calculated for the flow field. L_{xl} and L_{xt} denote the length scales from longitudinal and transversal correlation of velocity component U_x, respectively. L_{yl} and L_{yt} denote the length scales from longitudinal correlation and transversal correlation of velocity component U_y. L_{xl} and L_{xt} can be calculated using the expression below.

$$L_{xl}(x,y) = \int_0^{\zeta^*} G_{xl}(x, x+\zeta)d\zeta \quad (3)$$

$$L_{xt}(x,y) = \int_0^{\beta^*} G_{xt}(y, y+\beta)d\beta \qquad (4)$$

where G_{xl} and G_{xt} denote the coefficient for longitudinal and transversal correlation functions of U_x, respectively. They were calculated from the fluctuating velocity values at two separated positions (x, y) and (x + ζ , y) along x-axis or (x, y) and (x, y + β) along y-axis. ζ and β are the variable separation distances. ζ^* and β^* correspond to the first ζ and β value in auto-correlation function that make $G_{xl}(x, x+\zeta)$ and $G_{xt}(y, y+\beta)$ equal to zero. $G_{xl}(x, x+\zeta)$ and $G_{xt}(y, y+\beta)$ are expressed as:

$$G_{xl}(x, x+\zeta) = \frac{1}{N-1}\sum_{i=1}^{N} \frac{u_x(x,y,i)u_x(x+\zeta,y,i)}{u'_x(x,y)u'_x(x+\zeta,y)} \qquad (5)$$

$$G_{xt}(y, y+\beta) = \frac{1}{N-1}\sum_{i=1}^{N} \frac{u_x(x,y,i)u_x(x,y+\beta,i)}{u'_x(x,y)u'_x(x,y+\beta)} \qquad (6)$$

L_{yl} and L_{yt} were calculated in a similar way to that used to obtain L_{xl} and L_{xt} .

Shown in Fig. 6a is a typical raw Mie-scattered images of stoichiometric iso-octane/air flame at speed of 750 RPM. The dark region represents the presence of burned gas while the illuminated region is due to light scattered from the seeding particles and represents the unburned mixture. To minimize the light noise and detect the flame boundary accurately, an adaptive threshold was applied for image binarisation, in which a Gaussian lowpass filter was employed to generate a threshold map. The threshold for individual pixel was determined based on its neighbours' light intensity. Then, a Wiener filter was applied to the binarised image to eliminate the noise such as the intensity spike caused by incoming laser sheet. Eventually, a binarised flame contour with the raw image was produced, see Fig. 6b.

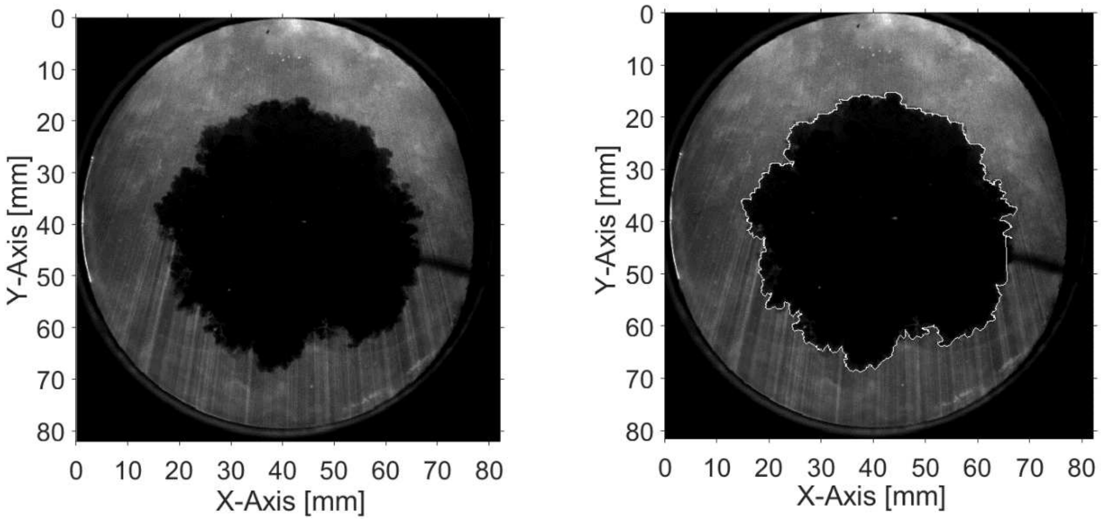

(a) (b)

Fig. 6: Illustration of a) Raw Mie-scattered image, b) Binarised flame contour with the raw image, for a stoichiometric iso-octane/air flame under 750 RPM. Axis unit [mm].

The flame shape was approximately circular, and the burned region centroid remained at the position of the spark kernel. As a result, the flame contour was treated as a symmetric object. The spark plug is located at the centroid of the contour. However, the spark stem (a metal wire appears as a dark line in the raw image) concealed a small part of the flame contour. To eliminate this error and any other rare imperfections, only top half section of the flame contour was used for analysing the flame wrinkling. The flame contour data were stored in a series orthogonal coordinates. To obtain the area of burned region, a flame contour was divided into equal sectors with an angle of 10° as shown in Fig. 7a. The area A_i of sector i (i = 1, 2, ...18) at time t, was obtained by integrating the dark region from top half of the image on the incident laser sheet side. The radius R_i of i-th sector, follows

$$R_i = \sqrt{\frac{360 A_i}{10\pi}} \quad (7)$$

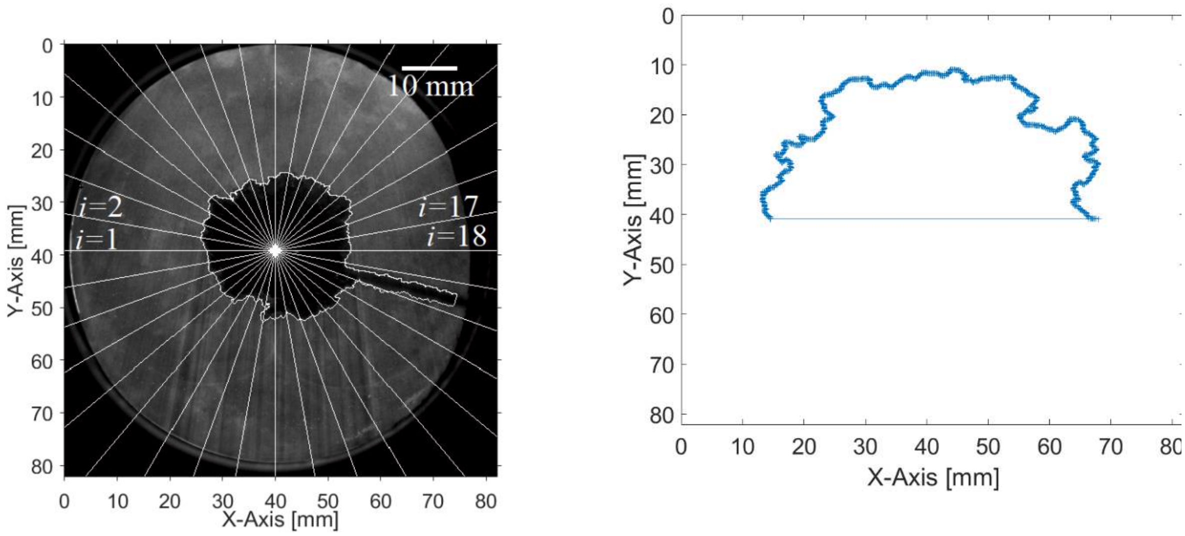

(a) **(b)**

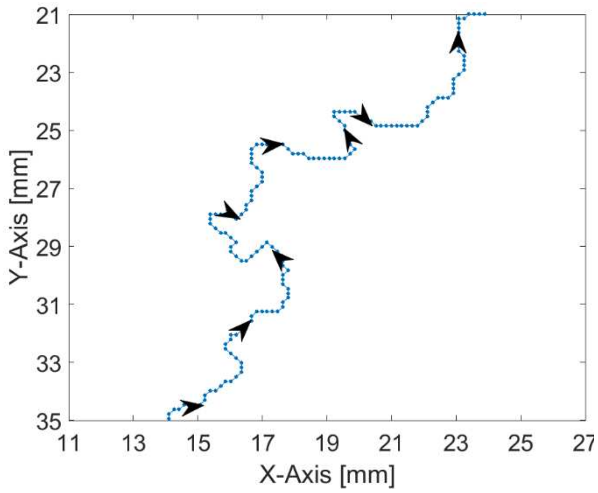

(c)

Fig. 7: Illustration of (a) flame contour evenly divided into 36 sectors, (b) flame contour formed via a clockwise contour coordinate (axis units [mm]), (c) a detailed flame contour coordinates in a grey square from (b).

The averaged flame radius $\bar{R}$ indicating a mean flame front was obtained by taking an arithmetic average of the 18 local sector flame radius R_i. The amplitude of flame wrinkling $a(s)$ along flame contour was given by the deviation of the local flame front from the mean flame front.

$$a(s) = R(s) - \bar{R} \tag{8}$$

where $R(s)$ is the instantaneous flame radius at compass spacing, s, along the flame contour. The compass spacing is the length of two adjacent pixels on flame contour. The mean $\bar{a}$ and the root-mean-square a' values of the flame edge fluctuation were defined as:

$$\bar{a} = \frac{1}{S}\int_0^S a(s)ds \tag{9}$$

$$a' = \sqrt{\frac{1}{M}\int_0^M [a(s) - \bar{a}]^2\, ds} \tag{10}$$

where M is half perimeter of the flame contour since only half of the flame image is used. From the amplitude of flame wrinkling, an integral scale of flame wrinkling L_a is obtained by autocorrelation function:

$$L_a = \int_0^M R_k(\xi)\, d\xi \tag{11}$$

$$R_k(\xi) = \frac{2}{S}\int_0^{M/2} a(s)a(s+\xi)\, ds \tag{12}$$

where $R_k(\xi)$ is spatial length correlation of fluctuating component between ξ separation distance.

2.4. Measurement uncertainty

A detailed measurement uncertainty has been presented in [29, 30] and a brief summary is provided here. The technique for measuring the velocities detailed within the presented work operates by recording the displacement of the flame front over a known time period. The inaccuracies that occur within this process are therefore linked to how precisely those positions can be ascertained in both time and space. The position of the flame fronts recorded using the PIV system can only be measured to the nearest pixel location due to the analysis routine used and digital nature of the recording, it is therefore dependent on the image area and camera resolution. For the case of the example data shown in section 2.3 the image size was 80 mm square, recorded using a high-resolution Photron AR-X camera which had a resolution of 512 by 512 pixels. As a result, the flame leading edge of the flame position, recorded at the isotherm where the oil particles are vaporised, can only be determined to within a tolerance of ±0.156 mm. The curvature of the flame perpendicular to the laser sheet will also induce a bias in flame position. This bias that varies depending on the location of the flame relative the bore centre. However, as both instances of flame front identification suffer from the same bias and the displacement of the flame between images is small, its effect on flame velocity measurement is very small, 0.16 mm in the worst case. Mean value of velocities were used, at each condition, to minimize the error in processing procedures. As a result, flame edge locations can only be determined to within an accuracy of ± 0.02 mm.

To also ensure that the particles are able to follow the flow and track it accurately, their relaxation time was calculated at each condition. This time should be less than the characteristic time scale [31]. For an olive oil particle of diameter 5 μm, this time was 2.8 μs which was very short and much less the integral time scale (section 3.1). With this selected size, the droplets were small and fast enough to follow the current flows. The selected size was also large enough to scatter sufficient light. The average number of particles for each interrogation window was about 10 - 34 particles within the optimized range, suggested by [31, 32]. This indicated that the seeding density inside the vessel during PIV measurements was just sufficient and not too much to influence the data processing, nor too small to provide absent velocity.

3. Results and Discussion

3.1. Turbulence Parameters in Motoring Cycles

Figure 8 shows the temporal and spatial variation of the turbulence RMS velocities, u'_x and u'_y, at engine speeds of 750 and 1500 RPM, based on 50 motoring cycles. Both velocities are in good agreement in terms of magnitude and tendency at crank angles between -10º and 30° after TDC (aTDC). Beyond this crank angle, they start to depart, possibly due to the relatively large piston velocity that reduces the homogeneity of in-cylinder turbulence. A characteristic turbulence RMS velocity, u' ($=u'_x= u'_y$) can be employed to represent the turbulence intensity as the flow field is, essentially, homogeneous in the two dimensions of measurement. To investigate the spatial variation of turbulence RMS velocity, u' was plotted, at 10º aTDC, on the radial distance from the spark, Fig. 8b. Only the distance between 5 mm and 35 mm was considered to eliminate the effect of spark plug and cylinder wall on turbulent flow. Figure 8b shows that the variation of u' along the radial direction is minor under both engine speeds. One can thus conclude that flow field within LUPOE-2D can be considered homogenous turbulence.

At speed of 750 RPM, the turbulence RMS velocities remain constant at a value of 0.75 m/s up to a crank angle of 20° aTDC. A constant RMS velocity indicates that the turbulence decay is compensated by other source of turbulence, e.g. induced by the piston movement in expansion stroke. However, this balance is broken due to the acceleration of piston as it moves beyond 20° aTDC. The rapid piston movement generates turbulence which increases the turbulence RMS velocities rapidly. In the case of 1500 RPM, both u'_x and u'_y plots do not show a notable plateau up to a crank angle of 35° aTDC. This is probably due to extra turbulences generated as engine doubles the speed, which makes the total turbulence level rise steadily. Meanwhile, turbulence RMS velocities are about 50% higher than those at 750 RPM across this duration. However, this might not be the sole reason [33-35].

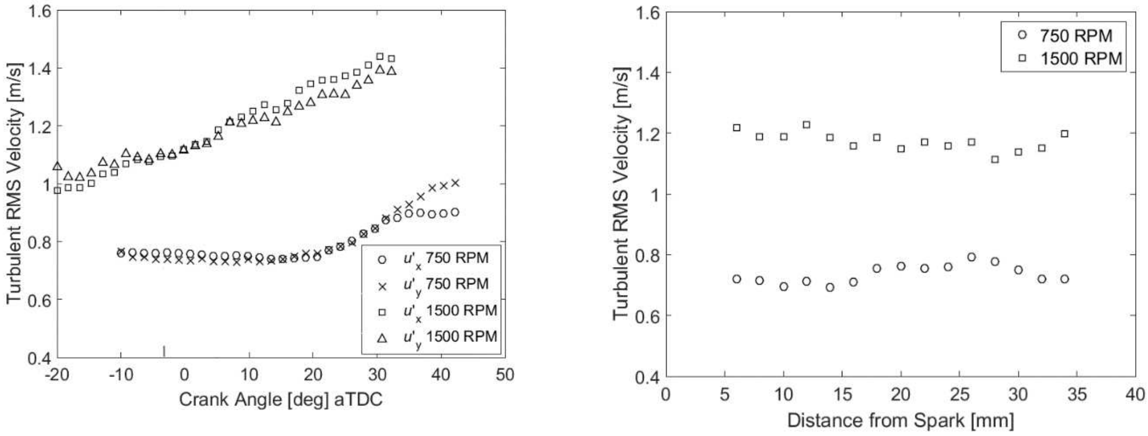

(a) (b)

Fig. 8: Variation of the turbulent RMS velocity, (a) Temporal, and (b) Spatial.

The longitudinal integral length scales (L_{xl} and L_{yl}) and transversal integral length scales (L_{yt} and L_{yt}) were plotted as a function of crank angles for 750 RPM and 1500 RPM, in Fig. 9. In general, the transversal integral length scales is about half of its longitudinal integral length scale for both engine speeds, as it is the case with homogenous turbulence [36]. Moreover, both longitudinal and transverse integral lengths increase slightly as engine doubles the speed. In addition, the discrepancy of length scale between two velocity directions is small, which reflects a homogenous turbulence within the motoring LUPOE-2D engine. Since the increment of length scale is minor as engine doubles the speed, a longitudinal integral length scale L_{xl} = 3.5 mm at 10º aTDC was selected as the characteristic turbulence length scale, L, for both engine speeds when non-dimensionalising the wrinkle parameters as discussed in Section 3.3.

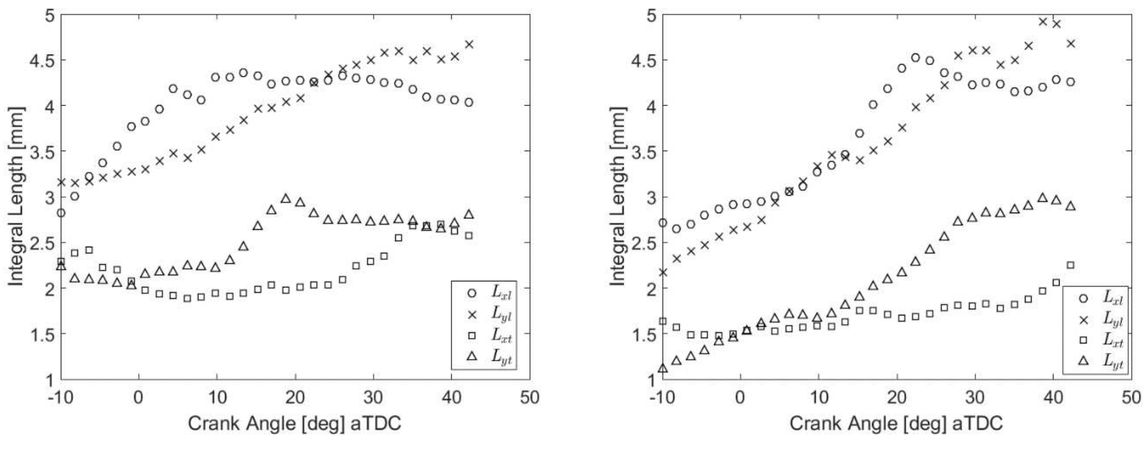

(a) **(b)**

Fig. 9: Variations of length scales with crank angle, at engine speeds of a) 750 RPM, b) 1500 RPM.

3.2. Observations of Turbulent Flame Propagation

Figure 10 provides a general observation of turbulent flame front contours. It clearly shows that the flame is nearly spherical in the early stage and it tends to grow non-uniformly in different sector during flame growth. Number of flame wrinkles increase as the flame grows larger. Highly wrinkled flames occur at engine speed 1500 RPM with $\phi = 0.8$ due to its highest ratio of u'/u_l compared to other conditions.

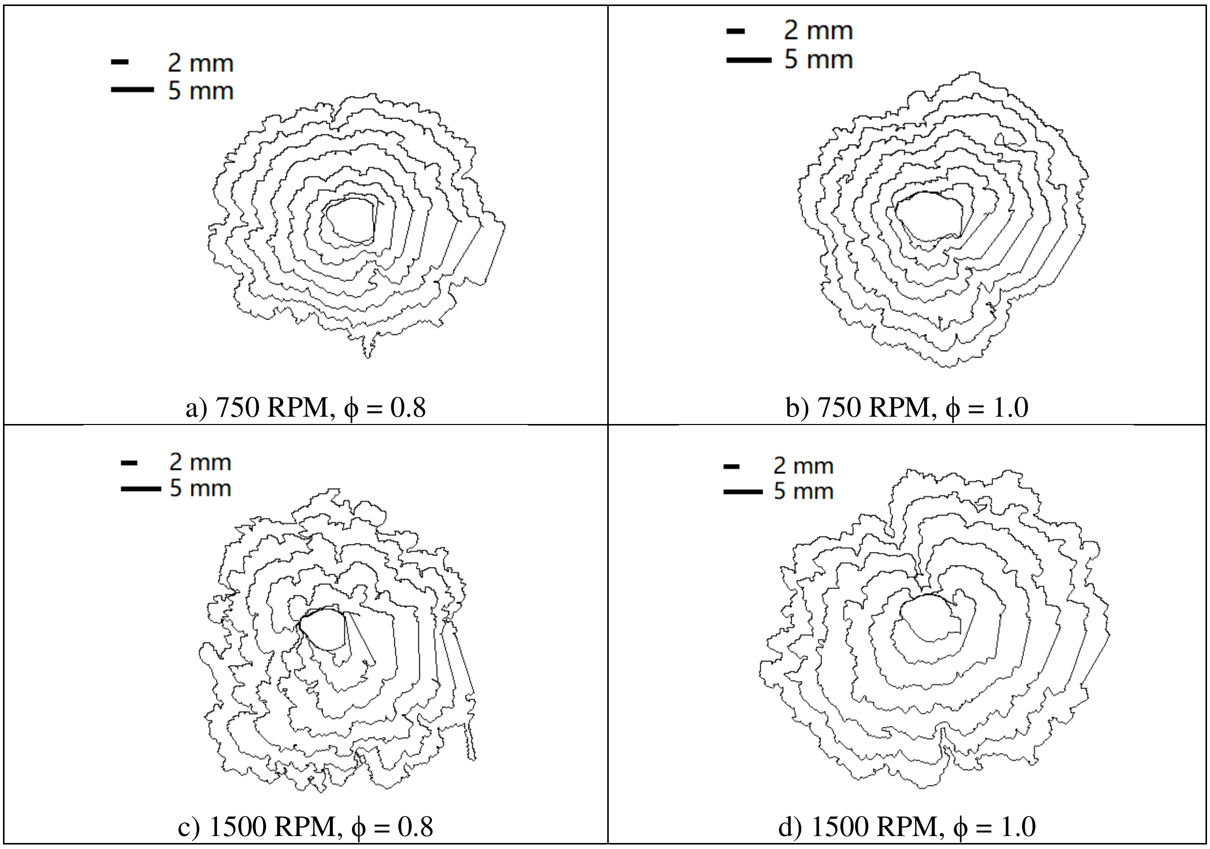

Fig. 10: Turbulent flame development history with a time interval of 0.3 ms for iso-octane under four different conditions.

From the flame contours in Fig. 10, the averaged flame radius, $\bar{R}$, was derived and plotted with respect to the time after ignition under four different conditions based on 30 firing cycles, in Fig. 11. The flame propagation inside LUPOE engine can be classified as three stages [38]: initial acceleration (0-10% fuel mass burned), fully developed (10-30% fuel mass burned) and deceleration stage (40-100% fuel mass burned) when the flame radius grows from 0 – 12 mm, 12 - 32 mm and 32 - 40 mm, respectively. Clearly, the flame radius curves for 1500 RPM feature a larger slope compared to those at 750 RPM, indicating a fast turbulence flame propagation speed induced by stronger turbulence. The discrepancy of curve slop between stoichiometric and lean mixture is notable at 1500 RPM, but becomes less pronounced at 750 RPM.

Note that the pixel resolution for a full-bore view is about 0.16 mm × 0.16 mm. This pixel size is too coarse to capture the smallest wrinkles at the range of Kolmogorov length scale (of the order of 0.01 mm) [39]. To investigate the flame surface structure in a detailed manner, a zoomed in laser sheet flame images were obtained with a pixel resolution of 0.065 mm × 0.065 mm, which is slightly above the inner cut-off scale ranged from 0.033 to 0.044 mm (see Table 3) for tested engine speeds and equivalence ratios. Four zoomed in views are shown in Fig. 12. Each illustrates one-quarter of a flame propagation at the conditions indicated. Such camera settings allow recording the whole one-quarter flame propagation up to a flame radius of 20 mm. Two pixels are necessary to minimally resolve structure of wrinkle. Hence, the smallest flame wrinkle resolved in Fig. 12 has a size of 0.13 mm. To resolve much smaller wrinkles of the same size of inner cut-off scale, it would need to zoom image in much more to obtain a pixel resolution of better than 0.050 mm. This is beyond the capabilities of existing technique.

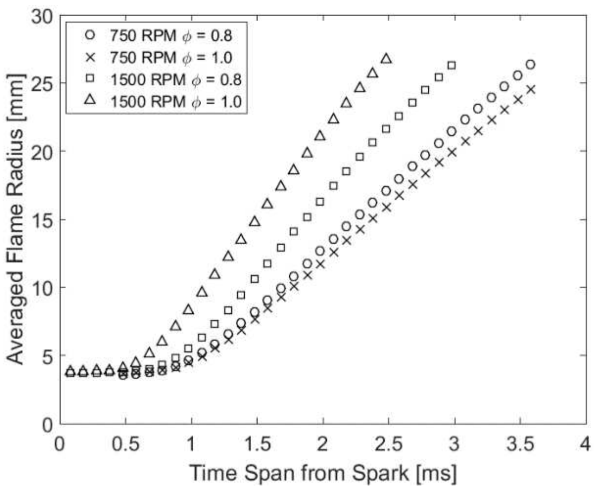

Fig. 11: Time evolution of averaged flame radius, $\bar{R}$, for iso-octane under four different conditions.

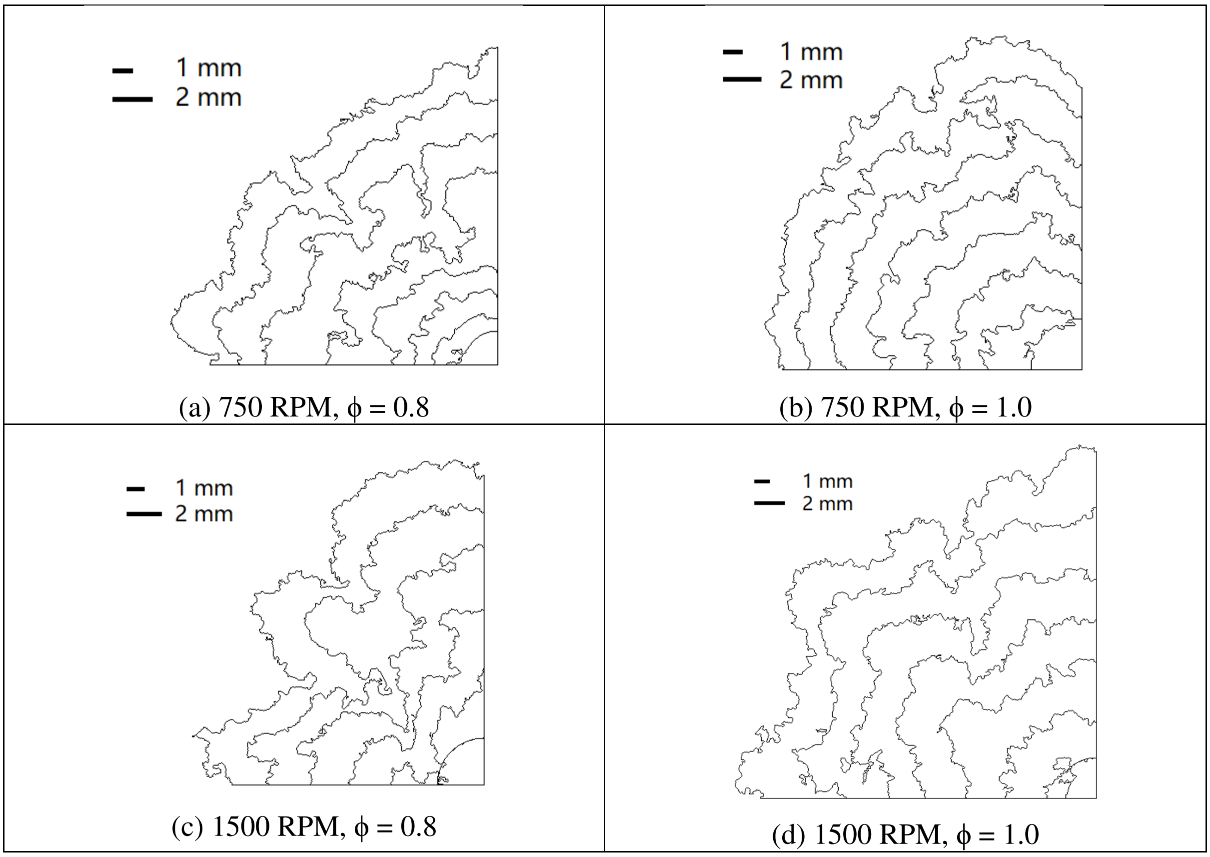

Fig. 2: Turbulent flame development history with 0.3 ms time interval for iso-octane under four different conditions, for camera zoomed-in cases.

3.3. Flame Wrinkling

Given the relatively symmetric and round flame contours, the flame surface wrinkles can be measured by a non-dimensional parameter, sphericity, that is defined as [40]:

$$\text{sphericity} = 4\pi A/P_e^2 \quad (13)$$

where A is the area of 2D flame contour. The length of flame contour P_e was determined by stepping along the whole flame boundary at a compass spacing [9].

Since only the top half part of the flame is considered, the values of A and P_e were obtained by doubling the top half part of the burnt gas region. Both the flame contour area and contour length increase as the flame front becomes more wrinkled. However, sphericity has an inverse root dependence on the flame contour length. This leads to a reduction in the flame sphericity. Value of sphericity varies from 0 to 1. A value of 1 indicates a spherical flame without wrinkling. A small value of sphericity indicates a highly wrinkled flame surface, hence a large surface area.

Flame sphericity for iso-octane/air mixtures is shown in Fig. 13. In general, the sphericity decreases as flame radius increases. This can be attributed to the increase in the flame front wrinkling during the initial stage (5-12 mm). Increasing engine speed or reducing equivalence ratio results in more winkled flame surfaces, thus a lower sphericity. During the fully developed stage (12-19 mm), the symbols for sphericity feature smaller slopes compared to the initial stage, indicating that the amount of wrinkling remains unchanged.

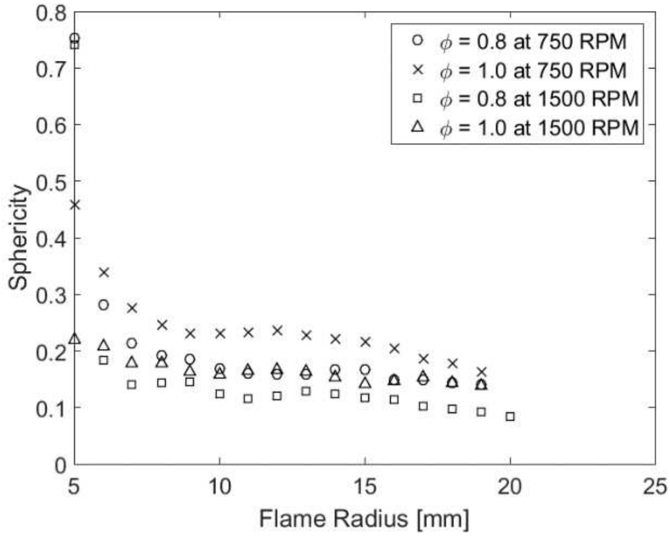

Fig. 3: Flame sphericity as a function of flame radius for iso-octane/air mixtures under four different conditions.

Figure 14a shows an example of the flame surface contours at three consecutive time instances for iso-octane at 750 RPM stoichiometric condition. The amplitude of local wrinkling, $a(s)$ was plotted along the flame contour, shown in Fig. 14b. Only a few large scale wrinkles present on the flame contours and wavelengths of some of the wrinkles are stretched with the expansion of flame. In order to analyse the profile of the winkling quantitatively, RMS amplitude of flame wrinkling, a' (Eq. 10) and integral length scale of wrinkling, L_a (Eq. 11) were compared and discussed under four different conditions. Presented in Fig. 14c is the development of a' as a function of flame radius. a' increases almost linearly with growth of flame radius indicating the wrinkle size increases during flame growth under any given engine conditions. In addition, the quantity of large wrinkles and their magnitude predominate the value of a'. And a' is less sensitive to the small wrinkles. Similar to sphericity, a' increases as engine speed increases or equivalence ratio decreases. For engine speed 1500 RPM, a notable discrepancy in a'

between stoichiometric and $\phi = 0.8$ indicates a pronounced effect of mixture strength under stronger turbulence condition.

Presented in Fig. 14d is the integral length scale of wrinkling, L_a as function of flame radius. In general, L_a increases linearly as the flame grows because the flame surface wrinkles stretched with flame expansion. It also suggests those wrinkles grow without changing the flame shape much. A relative large L_a appeared on a bigger flame contour indicates that the flame contour may have only a few very large wrinkles.

Comparing Fig. 14c and Fig. 14d, one can see that L_a is significantly larger than a' under any conditions. The value of L_a during the fully developed stage is about twice higher than the length scale of turbulence, *L*, measured in LUPOE-2D (comparing Fig. 14d and Fig. 9).

To analyse the spectral content of flame wrinkles, PSD was derived by the Fourier transform of wrinkling amplitudes, $a(s)$ at the fully developed stage. Figure 15 shows the spectral coefficient of PSD function, *S*, as a function of wave number, *k*, obtained from the present system and other systems reported by [6]. The operating characteristics (turbulence level, mixture strength) of each system and each condition are denoted by u'/u_l. Along the *x*-axis, the wavenumber of wrinkles falls within the range between 0.025 and 8 mm^{-1}, which corresponds to the largest scale close to the radius of engine bore (40 mm) and the smallest one just above the limit of image resolution (0.13 mm).

Clearly, the flame front is exposed to the full spectrum of turbulence length scales at the fully developed stage. The size of wrinkles is primarily determined by turbulence in front of flame and occasionally by inherited non-spherical flame shape produced early during flame development. Along the *y*-axis is the $S(k)$ in logarithmic scale. For the current system, all four PSDs coincide for a range of wave numbers (0.04 - 1 mm^{-1}) except a small discrepancy between 1-8 mm^{-1}. They also exhibit a similar trend as those of burner, bomb and naturally aspirated LUPOE engine that feature a relatively low operating pressure. In general, varying pressure alters the flame thickness and burning velocity. The higher the pressure, the greater the negative Markstein number. The appearance of cellular structures induced by negative Markstein number could enhance flame surface wrinkling in addition to those induced by turbulence, and thus influence the variation of PSD. However, all six data sets of PSD show a relatively high amount of scatter for the small wavenumbers, which are corresponding to large wrinkles. The majority of cellular structures occur at a small scale whose contribution to large wrinkles becomes less. This indicates that the majority of cellular structures occur at small scale whose contribution to large wrinkles becomes less. It is worthwhile to investigate the small wrinkles where the cellularity may make a notable contribution and affect the slop of PSD. However, to differentiate the small cellular structure from turbulence-induced wrinkles challenges the current laser and imaging system since the curvature of flame front needs to be derived. The spectral content of the flame wrinkles observed this work gets the practical purpose and sufficient for analysis.

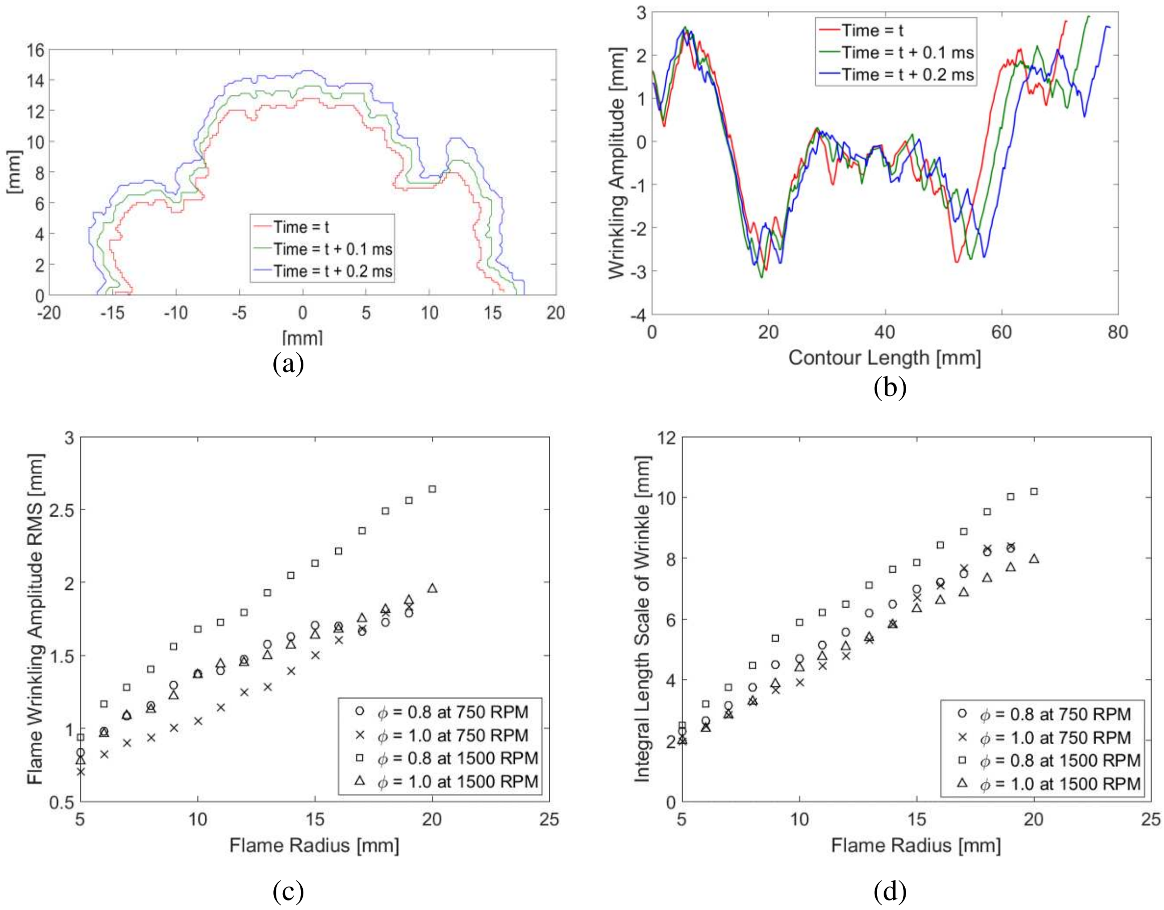

Fig. 4: An example of (a) consecutive flame contours with 0.1 ms time interval of iso-octane at 750 RPM stoichiometric condition, (b) amplitude of local wrinkling along the flame contour derived from (a), (c) RMS amplitude of flame wrinkling a', (d) integral length scale of flame wrinkling L_a with respect to flame radius under four different conditions.

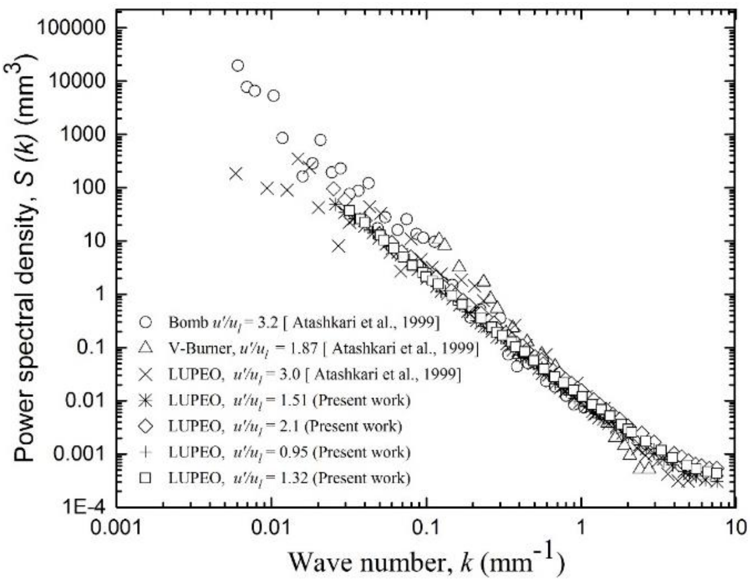

Fig. 5: Variation of power spectral density, *S*, with wave number, *k*.

Turbulent flame surface wrinkling arises from the motion of turbulent eddies. It is therefore interesting to compare the PSD of flame wrinkling with that for turbulence, which could provide a lot of useful information on the intrinsic link between flame wrinkling and turbulence energy cascade. The PSD of flame wrinkling has a steeper slop (-2.6) than that for isotropic turbulence within inertial sub-range in which the energy spectra exhibits a -5/3 decay measured from bomb [41], burner [20, 42]) and LUPOE engine [5]. This slope becomes gentler as wave number becomes greater than 1 mm, and starts to follow the -5/3 power law for wave numbers from 1 - 4 mm^{-1}. Beyond this point, this slope tends to flat out due to the limited image resolution causing difficulty in capturing much smaller wrinkles. Overall, the slope of the flame wrinkling spectrum follows the turbulence energy cascade in the inertial subrange, indicating the energy in wrinkles is solely from turbulence.

Gradients of the PSDs in all four cases are approximately -2.6 at the wave numbers < 0.3 mm^{-1}. This value is consistent with previous experimental findings [6] in which a value of -2.5 was observed for LUPOE, -2.7 for bomb, -3.2 for burner. All PSD's for each value of u'/u_l ($\in$ 0.95-3.2) nearly coincide with one another, suggesting that a generality of flame wrinkling development is possibly applicable for all premixed flames.

By analogy with the normalized spectrum of turbulence, Atashkari et al. [6] proposed a universal non-dimensional PSD of flame wrinkling using the wrinkling parameters, a_k' and L_{ak}. The normalisation of

$S(k)$ and k is by ${a'_k}^2 L_{ak}$ and L_{ak}, respectively. The resulting PSD curves, shown in Fig. 16, start to deviate for the wave number $k\,L_{ak}$ greater than 3. The present system exhibits the highest $S(k){a'_k}^2 L_{ak}$ value amongst compared to other systems. Note that the original method for normalizing spectrum of turbulence employed a fully developed u' and L. The values of a'_k and L_{ak} are increasing during flame growth, as shown in Figs. 14c and 14d. As stated by [6], it is not necessarily reasonable to assume the maximum attained a'_k and L_{ak} for normalization since they are not available for flames temporally developing within the engine. In addition, such a PSD becomes slow valueless for predicting the flame characteristics since a'_k and L_{ak} need to be known beforehand.

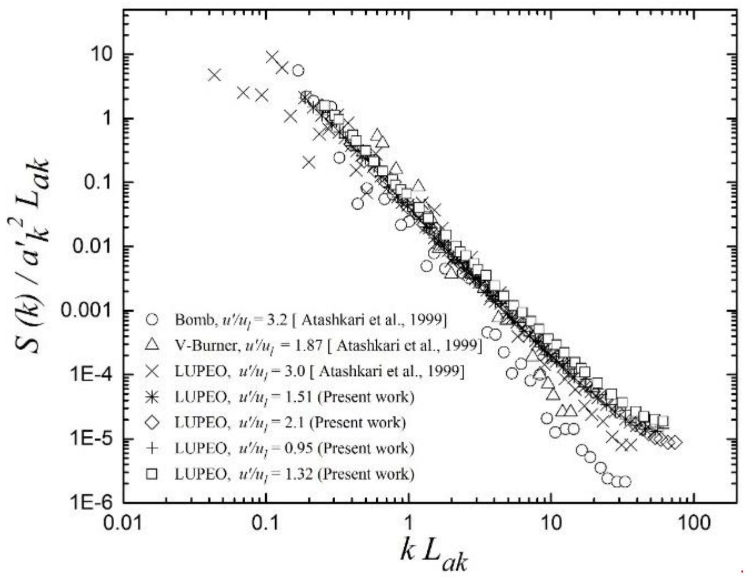

Fig. 6: Variation of normalised PSD, $S(k){a'_k}^2 L_{ak}$, with $k\,L_{ak}$.

Since turbulence predominates flame wrinkling, it appears reasonable to non-dimensionalised PSDs with the turbulence parameters u' and L. Hence, the second attempt is to normalize $S(k)$ and k by $L^3(\frac{u'}{u_l})^3$ and $L(\frac{u'}{u_l})$, respectively. The resulting non-dimensionalised wrinkling PSDs were presented in Fig. 15. The PSD's from different rigs were well discriminated over the whole spectrum. For example, all PSD's for engine system overlay each other, which demonstrates a pronounced generality of wrinkling characteristics for flames in this rig. Building on this reasonable correlation, the characteristics of flame wrinkling in each rig becomes predictable under any set of turbulence conditions. This correlation has weak connectivity to stretch since all measurements in Figs. 15, 16 and 17 were made under relatively low turbulence, hence stretch was low and not considered in the dimensionless groups. Under high turbulence level, stretch as being important for flame wrinkling to be examined carefully. In addition, this correlation excluded the flame thickness that is highly sensitive to the pressure and affects the smallest wrinkles. The higher the pressure, the thinner the flame, the smaller the wrinkle. Despite this, studies on this general correlation have provided important insights into the mechanisms of turbulent premixed flame wrinkling and paved the way for developing a comprehensive correlation in which turbulence-induced stretch and pressure-dependent flame thickness should enter into the dimensionless groups.

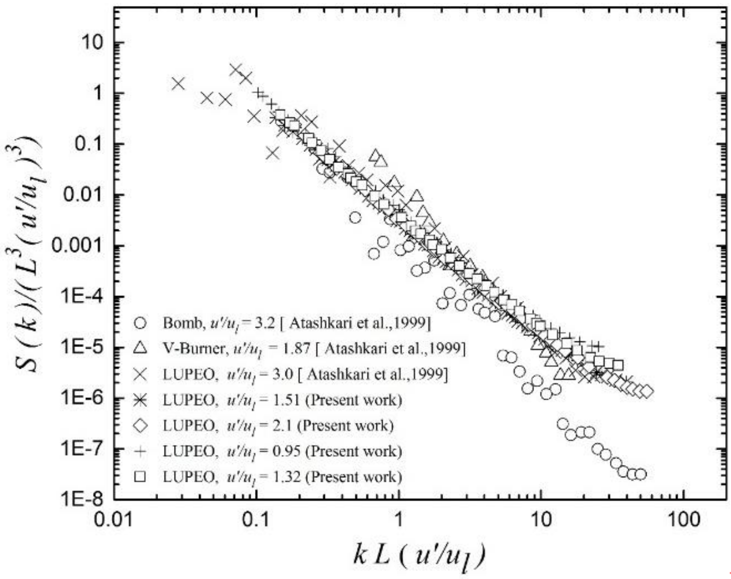

Fig. 7: Variation of normalised PSD, $S(k)/(L^3(u'/u_l)^3$, with $k\ L(u'/u_l)$.

4. Conclusion

1. The present work investigated the characteristics of flame wrinkling in a boosted LUPOE2-D engine. The turbulence parameters, u' and L, inside the engine were measured using PIV system under motoring cycles.
2. A homogenous turbulence was observed inside LUPOE2-D engine. The laser sheets used for PIV were also used to provide 2D Mie scattered images for detailed structure of flame surfaces during the firing cycles. The flame wrinkling parameters, a’ and La, were derived for iso-octane-air mixtures under various operating conditions.
3. Power spectral density functions of flame wrinkling obtained via Fourier Transform exhibited the same general trend under given conditions. They were found to be in remarkably good agreement with previous work measured from other rigs that featured lower pressures.

4. The present data were then non-dimensionalised in terms of wrinkling parameters and turbulence parameters, respectively. The generality map for turbulent flame wrinkling was updated by including the present work on the high-pressure regime. It is evident that turbulence-based normalization shows a pronounced generality of flame wrinkling from each rig.
5. The present work confirmed more confidently that this generality map is valid at pressure up to 30 bar. This generality map is valuable since flame spectra from each rig becomes predictable when turbulence parameters are known. However, further study will be required to extend this correlation for high turbulence regime. In addition, it will be necessary to investigate the curvature, stretch rate and flame thickness more carefully.

Acknowledgments

The authors are also grateful to Dr. Malcolm Lawes for useful discussions.

References

1. Lecointe, B. and Monnier, G. (2003) Downsizing a gasoline engine using turbocharging with direct injection. *SAE Technical Paper 2003-01-0542*. DOI: https://doi.org/10.4271/2003-01-0542
2. Driscoll, J.F. (2008) Turbulent premixed combustion: Flamelet structure and its effect on turbulent burning velocities. *Progress in Energy and Combustion Science*. 32(1), pp.91-134.
3. Bradley, D., Lawes, M., Liu, K. and Mansour, M.S. (2013) Measurements and correlations of turbulent burning velocities over wide ranges of fuels and elevated pressures. *Proceedings of the Combustion Institute*. 34(1), pp.1519-1526.
4. Wirth, M., Keller, P. and Peters, N. (1993) A flamelet model for premixed turbulent combustion in SI-engines. *SAE paper 932646*.
5. Hicks, R.A., Lawes M., Sheppard, C.G.W. and Whitaker, B.J. (1994) Multiple laser sheet imaging investigation of turbulent flame structure in a spark ignition engine. *SAE paper 941992*.
6. Atashkari, K., Lawes, M., Sheppard, C.G.W. and Woolley, R. (1999) Towards a general correlation of turbulent premixed flame wrinkling. *Engineering turbulence modelling and experiments.* 4, pp.805-814.
7. Boyer, L. (1980) Laser tomographic method for flame front movement studies. *Combustion and Flame*. 39(3), pp.321-323.

8. Takeno, T., Murayama, M., Tanida, Y. (1990) Fractal analysis of turbulent premixed flame surface. *Experiments in Fluids*. 10, pp.61-70.
9. Shepherd, I. G., Cheng, R. K., Talbot, L. (1992) Experimental Criteria for the Determination of Fractal Parameters of Premixed Turbulent Flames. *Experiments in Fluids*. 13, pp.386-392.
10. Gülder, Ö.L. and Smallwood, G.J. (1995) Inner cutoff scale of flame surface wrinkling in turbulent premixed flames. *Combustion and Flame*. 103(1), pp.107-114.
11. Haq, M.Z., Sheppard, C.G.W., Woolley, R., Greenhalgh, D.A., Lockett, R.D. (2002) Wrinkling and curvature of laminar and turbulent premixed flames. *Combustion and Flame*. 131(1), pp.1-15.
12. Bradley, D., Lawes, M. and Morsy, M.E. (2021) Combustion-induced turbulent flow fields in premixed flames. *Fuel*. *290*, p.119972.
13. Cohé, C., Halter, F., Chauveau, C., Gökalp, I., Gülder, Ö.L. (2007) Fractal characterisation of high-pressure and hydrogen-enriched CH4–air turbulent premixed flames. *Proceedings of the Combustion Institute*. 31(1), pp.1345-1352.
14. Suzuki, K. and Nishiwaki, K. (2003) Fractal Dimension Growth in Flame Front Wrinkles during the Early Phase of Flame Propagation in an SI Engine. *SAE Technical Paper 2003-01-1840*. https://doi.org/10.4271/2003-01-1840.
15. Nomura, Y. and Shimizu, R. (2005) Fractal Analysis of Flame Front in a SI engine. *The Proceedings of the Thermal Engineering Conference*. pp.351-352.DOI:10.1299/jsmeted.2005.351
16. Köhler, J., Ziegler, G.F.W., Herweg, R., Meinhardt, P. (1992) 2-Dimensional Flame Contour Analysis in a Spark Ignition Engine. *Proceedings of 25th International Symposium on Automotive Technology and Automation*.
17. Kobayashi, H. and Kawazoe, H. (2000) Flame instability effects on the smallest wrinkling scale and burning velocity of high-pressure turbulent premixed flames. *Proceedings of the Combustion Institute*. 28(1), pp.375-382.
18. Gashi, S., Hult, J., Jenkins, K.W., Chakraborty, N., Cant, S., Kaminski, C.F. (2005) Curvature and wrinkling of premixed flame kernels—comparisons of OH PLIF and DNS data. *Proceedings of the Combustion Institute*. 30, pp.809–817.

19. Weiß, M., Zarzalis, N. and Suntz, R. (2008) Experimental study of Markstein number effects on laminar flamelet velocity in turbulent premixed flames. *Combustion and Flame*. 154(4), pp.671–691.

20. Kheirkhah, S. and Gülder, Ö.L. (2013) Turbulent premixed combustion in v-shaped flames: Characteristics of flame front. *Physics of Fluids*. 25(5):055107.

21. Ling, Z. (2014) Flame propagation and autoignition in a high pressure optical engine. PhD Thesis, University of Leeds, pp. 66-79.

22. Ichikaw, A., Naito, Y., Hayakawa, A., Kudo, T., Kobayashi, H. (2019) Burning velocity and flame structure of CH_4/NH_3/air turbulent premixed flames at high pressure, *International Journal of Hydrogen Energy*. 44(13), pp.6991-6999.

23. Ling, Z., Burluka, A.A. and Azimov, U. (2014) Knock Properties of Oxygenated Blends in Strongly Charged and Variable Compression Ratio Engines. *SAE Technical Paper 2014-01-2608*.

24. Metghalchi, M. and Keck, J.C. (1982) Burning velocities of mixtures of air with methanol, isooctane, and indolene at high pressure and temperature. *Combustion and Flame*. 48, pp.191-210.

25. Roth, G.I. and Katz, J. (2001) Five techniques for increasing the speed and accuracy of PIV interrogation. *Measurement Science and Technology*. 12(3), p.238.

26. Thielicke, W., Stamhuis, E. J. (2014). PIV lab-towards user-friendly, affordable and accurate digital particle image velocimetry in matlab, *Journal of Open Research Software*. 2(1), p.e30.

27. Reuss, D.L., Zhong, Z., Yang, X., Kuo, T.W. and Sick, V. (2018) Measured and les motored-flow kinetic energy evolution in the TCC-III engine. *SAE Technical Paper No. 2018-01-0192*.

28. Bradley, D., Lawes, M. and Morsy, M.E. (2019) Measurement of turbulence characteristics in a large scale fan-stirred spherical vessel. *Journal of Turbulence*. 20(3), pp.195-213.

29. Zhang, W. (2018) Measurements of flow and combustion in a strongly charged spark ignition engine (Doctoral dissertation, University of Leeds).

30. Morsy, M.E.M.H. (2019) Studies of laminar and turbulent combustion using particle image velocimetry (Doctoral dissertation, University of Leeds).

31. Raffel, M., Willert, C.E., Scarano, F., Kähler, C.J., Wereley, S.T. and Kompenhans, J. (2018) Particle image velocimetry: a practical guide. Springer.

32. Melling, A. (1997) Tracer particles and seeding for particle image velocimetry. *Measurement science and technology*. 8(12), p.1406.

33. Ding, C.P., Peterson, B., Schmidt, M., Dreizler, A. and Böhm, B. (2019) Flame/flow dynamics at the piston surface of an IC engine measured by high-speed PLIF and PTV. *Proceedings of the Combustion Institute*. *37*(4), pp.4973-4981.

34. Peterson, B., Baum, E., Dreizler, A. and Böhm, B. (2019) An experimental study of the detailed flame transport in a SI engine using simultaneous dual-plane OH-LIF and stereoscopic PIV. *Combustion and Flame*. *202*, pp.16-32.

35. Morsy, M.E. and Yang, J. (2021) Numerical and experimental study on turbulence statistics in a large fan-stirred combustion vessel. *Experiments in Fluids*. 62(5), pp.1-20.

36. Zentgraf, F., Baum, E., Böhm, B., Dreizler, A. and Peterson, B. (2016) On the turbulent flow in piston engines: Coupling of statistical theory quantities and instantaneous turbulence. *Physics of Fluids*. *28*(4), p.045108.

37. Aleiferis, P.G., Behringer, M.K. and Malcolm, J.S. (2017) Integral Length Scales and Time Scales of Turbulence in an Optical Spark-Ignition Engine. *Flow, Turbulence and Combust.* 98, pp. 523–577.

38. Liu, K., Burluka, A.A. and Sheppard, C.G.W. (2013) Turbulent flame and mass burning rate in a spark ignition engine. *Fuel*. 107, pp. 202-208.

39. Lumley, J.L. (1999) Engines – an introduction, Chapter 5. Flow in the Cylinder, Cambridge University Press.

40. Russ, J.C. and Neal, F.B. (2016) The image processing handbook. 7th Edition, CRC press, ISBN 9781138747494.

41. Scott, M.J. (1992) Distributions of strain rate and temperature in turbulent combustion. PhD thesis, Department of Mechanical Engineering, The University of Leeds. pages. 12-13&130.

42. Kobayashi, H. (2002) Experimental study of high-pressure turbulent premixed flames. *Exper. Therm. Fluid Sci.* 26, pp.375–387.